Real-Time Water Vapor Maps from a GPS Surface Network: Construction, Validation, and Applications

SIEBREN DE HAAN AND IWAN HOLLEMAN

Royal Netherlands Meteorological Institute, De Bilt, Netherlands

ALBERT A. M. HOLTSLAG

Wageningen University, Wageningen, Netherlands

(Manuscript received 29 April 2008, in final form 1 December 2008)

ABSTRACT

In this paper the construction of real-time integrated water vapor (IWV) maps from a surface network of global positioning system (GPS) receivers is presented. The IWV maps are constructed using a two-dimensional variational technique with a persistence background that is 15 min old. The background error covariances are determined using a novel two-step method, which is based on the Hollingsworth–Lonnberg method. The quality of these maps is assessed by comparison with radiosonde observations and IWV maps from a numerical weather prediction (NWP) model. The analyzed GPS IWV maps have no bias against radiosonde observations and a small bias against NWP analysis and forecasts up to 9 h. The standard deviation with radiosonde observations is around 2 kg m^{-2}, and the standard deviation with NWP increases with increasing forecast length (from 2 kg m^{-2} for the NWP analysis to 4 kg m^{-2} for a forecast length of 48 h). To illustrate the additional value of these real-time products for nowcasting, three thunderstorm cases are discussed. The constructed GPS IWV maps are combined with data from the weather radar, a lightning detection network, and surface wind observations. All cases show that the location of developing thunderstorms can be identified 2 h prior to initiation in the convergence of moist air.

1. Introduction

At present, radiosonde observations are the most important operational source for upper-air water vapor data. These observations are expensive and thus are sparse in time and space. Global positioning system (GPS) zenith total delay (ZTD) observations contain integrated water vapor path information, which can be used in numerical weather prediction (NWP) models and for nowcasting severe weather. Assimilation of GPS observations has a positive impact on the quality of an NWP model (Macpherson et al. 2007; Poli et al. 2007; Smith et al. 2007). These high-temporal-resolution water vapor measurements are likely to also have a large impact on forecasting (rapidly) developing systems (Mazany et al. 2002; de Haan et al. 2002, 2004; de Haan 2006). Note that the method presented by Mazany et al. (2002) has a lead time of around 12 h.

The current measurements of atmospheric water vapor by the radiosonde network do not possess the temporal or the spatial resolution to provide adequate information about atmospheric scales that are smaller than synoptic scales. GPS radio occultation observations contain information on upper-air humidity; however, these observations are, in fact, combined temperature and humidity measurements, and the two can only be separated with additional information (e.g., temperature profile). Imagery from geostationary satellites provides more frequent monitoring of the atmospheric water vapor, but the use of these observations in NWP is complicated because of problems with height assignment of the observed structures and because of cloud contamination. These observations are very well suited for use in nowcasting. Because of use of passive sensors, however, lower-stratospheric water vapor information is confounded by overlying clouds or water vapor and is therefore only valid in cloud-free situations. Humidity

Corresponding author address: Siebren de Haan, Royal Netherlands Meteorological Institute, P.O. Box 201, 3730 AE De Bilt, Netherlands.
E-mail: siebren.de.haan@knmi.nl

DOI: 10.1175/2008JAMC2024.1

observations obtained from infrared and microwave sounders from polar-orbiting satellites suffer from the same problem. On the other hand, GPS can observe integrated water vapor (IWV) almost continuously, independent of clouds and rain.

In this paper a method of constructing GPS IWV maps from GPS observations is presented. These maps are validated with radiosonde observations, NWP-derived integrated water vapor, and GPS IWV estimated using a different processing network. Assimilation in NWP is, of course, another way of presenting the data to the forecasters. However, numerical weather model data generally have lead times of several hours. In this paper, we show that the real-time analysis of GPS observations can be used to bridge this gap. By discussing three cases, the application for nowcasting of thunderstorms is illustrated. First, a description of the data used is given. Next, the method of constructing two-dimensional IWV maps based on variational techniques is introduced. This is followed by a validation of the constructed IWV maps. Then, three cases of thunderstorm events in the Netherlands are presented.

2. Observations and infrastructure

A GPS receiver measures the delay of the GPS signal for every GPS satellite in view. By processing all observed slant delays within a certain time window, errors and unknowns, such as satellite and receiver clock errors, can be estimated. An estimate of the ZTD, which is the slant delay mapped to the zenith, is determined for each GPS receiver in the network. The hydrostatic part of the ZTD, called the zenith hydrostatic delay (ZHD), which is the vertical integral of dry air density, can be estimated using the surface pressure (Saastamoinen 1972). The residual part of ZTD is associated with the vertically integrated column of water vapor overlying the GPS receiver; that is,

$$\mathrm{IWV} = k^{-1}(\mathrm{ZTD} - \mathrm{ZHD}), \tag{1}$$

where k depends on the weighted mean temperature of the atmosphere, which in turn can be approximated by a linear function of the surface temperature (Davis et al. 1985; Bevis et al. 1994; Baltink et al. 2002).

General-application GPS receivers, such as those for time synchronization and car navigation, use (inexpensive) single-frequency receivers. The network of GPS double-frequency receivers used here was initially constructed for operational geodetic applications (land surveying; leveling); the network is presented in Fig. 1 (denoted by the black dots). Using two frequencies, the path delay due to the ionosphere can be eliminated. Data from this network are processed by the Royal Netherlands Meteorological Institute (KNMI) every 15 min; the observations are available approximately 5 min after observation time.

In this study, data from a different network are used in addition to the GPS data from the real-time network GPS. The additionally used estimates are processed on a routine basis by the Geodetic Observatory Pecny (GOP), in the Czech Republic, within the framework of the Network of European National Meteorological Services (EUMETNET) GPS Vapor Programme (E-GVAP). GOP estimates the atmospheric delay two times per hour; at the start and at the end of each window of 1 h. The network does not overlap with the real-time sites and thus samples different parts of the atmosphere and uses different GPS receivers (denoted by the stars and squares in Fig. 1). Both processing schemes use double differencing to eliminate clock errors. Some details of the processing options of the two schemes are shown in Table 1.

a. Radiosonde

The current system used is a Vaisala, Inc., RS92 radiosonde. This radiosonde has measurement uncertainties (based on experiments) of 0.1°C for temperature, 0.2 hPa for pressure, and 2% for relative humidity (Vaisala 2006) and is launched from De Bilt, in the Netherlands, at 0000 and 1200 UTC. De Bilt is denoted by the large cross in Fig. 1. Besides measurements of temperature and humidity, information on the wind speed and direction is inferred from the change in position of the balloon during its ascent. The current system uses a GPS receiver to track the balloon.

b. Weather radar

A weather radar employs scattering of radio-frequency waves (5.6 GHz/5 cm for C band) to measure precipitation and other particles in the atmosphere [see Doviak and Zrnić (1993) for more details]. The intensity of the atmospheric echoes is converted to the so-called radar reflectivity Z using the equations for Rayleigh scattering. The Rayleigh equations are valid when the wavelength of the radar is much larger than the diameter of the scatterers (maximum 6 mm for rain). In that case, the radar reflectivity depends strongly (to the sixth power) on the diameter of the rain droplets. The radar reflectivity is a good measure of the strength of the convection (updrafts) and the amount of condensed moisture in the atmosphere.

KNMI operates two identical C-band Doppler weather radars made by SELEX Sistemi Integrati (SELEX SI). The radar in De Bilt is located at 52.10°N, 5.18°E. The radar in Den Helder is located at 52.96°N, 4.79°E.

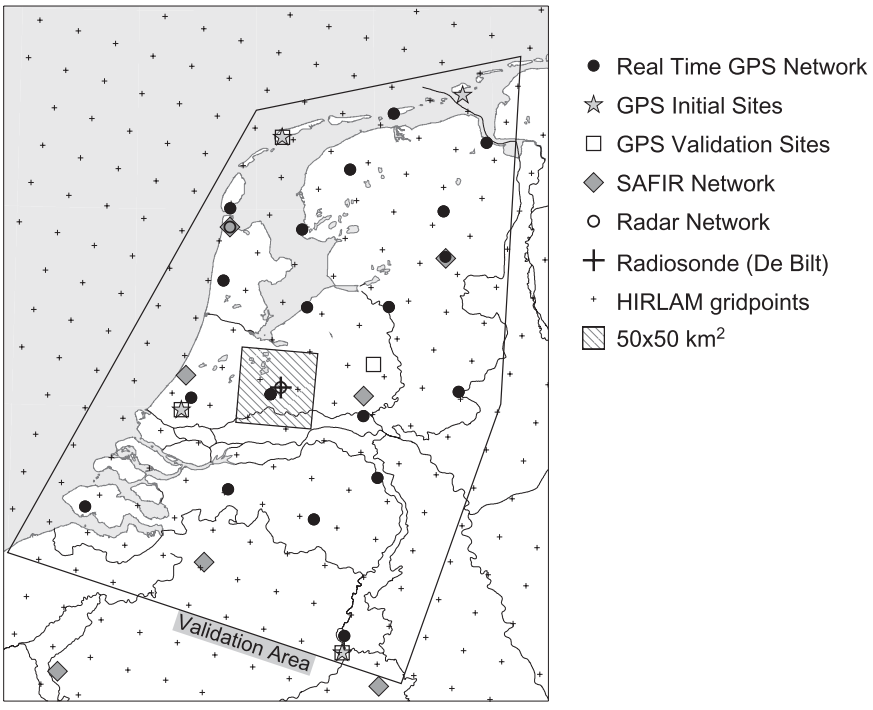

FIG. 1. Location of GPS sites, SAFIR antennas, two weather radars, and the radiosonde launch site. The crosses denote the HIRLAM grid points. Statistics against HIRLAM are derived within the validation area (large area), and the dashed area around the radiosonde launch site at De Bilt is used in section 4a.

The locations of the weather radars are designated in Fig. 1 by the open circles. The weather radars have recently been upgraded with digital receivers and a centralized product generation. Precipitation and wind are observed with a 14-level elevation scan (between 0.3° and 25°) that is repeated every 5 min.

From the three-dimensional scans, pseudo CAPPI images, that is, horizontal cross sections of radar reflectivity at constant altitude, are produced with a target height of 800 m above antenna level and a horizontal resolution of 2.4 km. Radar reflectivity values are converted to rainfall intensities R using a Z–R relationship (Marshall and Palmer 1948):

$$Z = 200R^{1.6}, \tag{2}$$

with the radar reflectivity Z in millimeters raised to the sixth power per meter cubed and rainfall rate R in millimeters per hour. More details on the KNMI weather radar network can be found in Holleman (2005, 2007).

c. Lightning detection network

KNMI maintains a Surveillance et Alerte Foudre par Interférométrie Radioélectrique (SAFIR) Lightning Detection System for monitoring (severe) convection and for feeding a climatological database. The lightning detection system consists of four detection stations located in the Netherlands and a central processing unit located at KNMI in De Bilt. In addition to the four Dutch stations, raw data from three Belgian stations operated by the Royal Meteorological Institute of Belgium are processed in real time as well. The locations of the seven detection stations are shown in Fig. 1 (gray diamonds).

Each lightning detection station consists of three basic components: a VHF antenna array, a low-frequency

TABLE 1. GPS processing options for GOP and KNMI. Both processing schemes use Bernese 5.2 software. Note that the observations window of KNMI is not constant over an hour. The start time of the window is kept constant for an hour; the end time changes every 15 min.

	GOP	KNMI
No. of sites	51	28
ZTD estimates	Hourly	Every 15 min
Min/max baseline (km)	23/3723	25/1653
Min elev cutoff angle (°)	10	10
Obs interval (s)	30	180
Obs window length (h)	12	11.25–12
Mapping function	Hydrostatic Niell	Hydrostatic Niell
Ocean tide loading	Scherneck (1991)	Ray (1999)

(LF) sensor, and a single-frequency GPS receiver. The VHF antenna array consists of five dipole antennas mounted in a circle and is used for the azimuth determination of discharges based on interferometry. The capacitive LF antenna is used for lightning discrimination, that is, cloud-to-ground (CG) or cloud-to-cloud discharge, and for time-of-arrival localization of CG discharges. The GPS receiver provides accurate time stamps for the observed discharges. The observed lightning events are localized by the central processing unit, and they are distributed in real time to the users.

The localization accuracy of the SAFIR network over the Netherlands is around 2 km. The false-alarm rate of the SAFIR network has been assessed using an overlay with weather radar imagery and is less than 1%. The detection efficiency for lightning events of the network is unknown and is currently under investigation. More details on the technical layout of the SAFIR network and its performance can be found in Beekhuis and Holleman (2004) and Holleman et al. (2006).

d. Numerical weather model data

At KNMI, a High-Resolution Limited Area Model (HIRLAM; Undén et al. 2002) is run operationally. This NWP model is started every 6 h and has a forecast length of 48 h. For the period under consideration, the model had a resolution of 22 km and 40 vertical levels. Synoptic observations, such as wind, temperature, and humidity from radiosondes and surface wind and temperature observations, are used to analyze the initial state of the atmosphere; note that no GPS data were assimilated. The previous 6-h forecast is used as background information and, because the model is a limited-area model, the forecast at the boundaries of the region is retrieved from the European Centre for Medium-Range Weather Forecasts forecast fields.

3. Construction of integrated water vapor fields

An objective analysis of total water vapor columns can be constructed in various ways. The simplest method is to horizontally interpolate between the observed values. This method is straightforward but assumes that the observations do not contain an error. Because all observations contain errors, an approach that incorporates these errors and correlations thereof is more appropriate. The method chosen here is based on a variational technique (see Daley 1991) that requires a background field and knowledge about the background error and observation error covariances. The optimal analysis $\mathbf{x}_a$ is determined by minimization of a cost function J given a background field $\mathbf{x}_b$:

$$J(\mathbf{x}) = (\mathbf{x} - \mathbf{x}_b)^{\mathrm{T}}\mathbf{B}^{-1}(\mathbf{x} - \mathbf{x}_b) + [\mathbf{y} - H(\mathbf{x})]^{\mathrm{T}}\mathbf{R}^{-1}[\mathbf{y} - H(\mathbf{x})], \quad (3)$$

where $\mathbf{x}$ is the state space with dimension $L = M \times N$ with grid sizes M and N, the vector $\mathbf{y}$ of dimension $\boldsymbol{K}$ are the observations, $\mathbf{B}$ is the background error covariance matrix ($L \times L$), $\mathbf{R}$ is the observation error covariance matrix ($K \times K$), and observation operator H maps the state space to the observations.

The state vector $\mathbf{x}$ represents the two-dimensional integrated water vapor field; the observations are IWV from GPS at a receiver location. This implies that the observation operator H is an interpolation of the water vapor field to the observation location. Here, a bilinear interpolation ($\mathbf{H}$) is chosen, which implies that the cost function J is linear and thus the optimal solution $\mathbf{x}_a$ can be determined analytically; that is, $\nabla J(\mathbf{x}_a) = 0$:

$$\begin{aligned} 0 &= \mathbf{B}^{-1}(\mathbf{x}_a - \mathbf{x}_b) - \mathbf{H}^{\mathrm{T}}\mathbf{R}^{-1}(\mathbf{y} - \mathbf{H}\mathbf{x}_a) \\ \Leftrightarrow \mathbf{x}_a &= (\mathbf{B}^{-1} + \mathbf{H}^{\mathrm{T}}\mathbf{R}^{-1}\mathbf{H})^{-1}(\mathbf{B}^{-1}\mathbf{x}_b + \mathbf{H}^{\mathrm{T}}\mathbf{R}^{-1}\mathbf{y}) \\ &= f(\mathbf{y}, \mathbf{x}_b; \mathbf{B}, \mathbf{R}). \end{aligned} \quad (4)$$

Integrated water vapor observations are available every 15 min, and thus an analysis with the same frequency is possible.

The matrices $\mathbf{B}$ and $\mathbf{R}$ play a key role in the analysis. Observation errors are correlated as a result of the method of observing (i.e., processing GPS signals). However, in the following it is assumed that these correlations can be neglected. The validity on this assumption needs to be investigated but is not discussed here.

Estimation of the background error covariances is a delicate matter. A common method of determining these covariances uses a forward model (such as an NWP model). The covariances are determined from the difference between the model forecast and the observations. This method is known as the Hollingsworth–Lonnberg method (Hollingsworth and Lonnberg 1986). The background error is then closely related to the forward model. For the system used here, no forward model is available that can provide a background estimate at analysis time for the variational system. Instead, the variational system is set up using a persistence background, and thus the error covariances between the observations and the background should be determined with a similar relation (i.e., persistence). How can a good estimate of the background error covariance be found without a forward model? We solved this problem by applying a two-step approach for the determination of a background error covariance for a persistence variational analysis scheme. The difference between the steps

lies in the origin of the background; the first background field will be a mean value valid at observation time, and the second one will have a time difference of 15 min. The estimate of the background error covariances based on the last background field will be used in the final real-time variational analysis scheme.

In the first step, the background is equal to a mean IWV value as observed by GOP (i.e., a single value for the whole domain). The locations of these GOP sites are indicated as gray stars in Fig. 1. Time series of offsets between the real-time observations and this background are used to determine the initial background error covariances $\mathbf{B}^0$; that is,

$$\mathbf{B}^0_{ij} = \overline{[\mathbf{IWV}^{\text{mean}}_i(t) - \mathbf{y}_i(t)][\mathbf{IWV}^{\text{mean}}_j(t) - \mathbf{y}_j(t)]^{\text{T}}}, \quad (5)$$

where $\mathbf{IWV}^{\text{mean}}_i(t)$ is the value at t as observed by GOP (the subscript i denotes the interpolation to the GPS site locations). The covariances are shown in Fig. 2a. Also shown in Fig. 2 is a fit of the background error covariance. Note that the value at zero distance actually is the sum of the background error and the observation error. Using this background, an initial analysis $\mathbf{x}^0_a$ can be constructed; that is,

$$\mathbf{x}^0_a(t) = f[\mathbf{y}(t), \mathbf{IWV}^{\text{mean}}(t); \mathbf{B}^0, \mathbf{R}]. \quad (6)$$

In the second step, the background is the initial analysis as obtained in the first step (using background error covariances $\mathbf{B}^0$). The time series of the differences between this analysis and observations 15 min later are used to determine the background error covariances $\mathbf{B}^1$:

$$\mathbf{B}^1_{ij} = \overline{[\mathbf{x}^0_{a,i}(t) - \mathbf{y}_i(t + 15')][\mathbf{x}^0_{a,j}(t) - \mathbf{y}_j(t + 15')]^{\text{T}}}, \quad (7)$$

where $\mathbf{x}^0_{a,i}(t)$ is the vector of initial analyses interpolated to locations at which the observations were recorded. The results are shown in Fig. 2b. The background error covariances $\mathbf{B}^1$ will be used to calculate the real-time variational analysis $\mathbf{x}_a$; that is,

$$\mathbf{x}_a(t) = f[\mathbf{y}(t), \mathbf{x}_a(t - 15'); \mathbf{B}^1, \mathbf{R}]. \quad (8)$$

The period over which the background error covariances are estimated runs from January to July of 2007. The background error covariance in the first step has values ranging from -2 to 6 kg m^{-2} for distances larger than zero. This is due to the coarse background field used, which is a single value for the whole region. The background error covariances decrease to values ranging from -1 to 1.5 kg m^{-2} in the second step. This decrease is the result of a better background estimate, although persistence is used and no forward model is applied. The estimate of the observation errors, which can be deduced from the covariances at zero distances, ranges from 1 to 1.5 kg m^{-2}. These values have been observed in earlier studies and show that the method used here results in good covariances (Rocken et al. 1993, 1995, 1997; Emardson et al. 1998, 2000; Liou et al. 2001; Niell et al. 2001; Stoew et al. 2001; Guerova et al. 2003).

4. Validation of integrated water fields

In this section the validation of IWV analysis fields is discussed. First, an example is presented that shows that the sudden development of a thunderstorm could not be forecast from time series information alone. Next, the quality of the IWV analysis fields is investigated.

a. Time series analysis

An example of the data described previously is shown in Fig. 3 for 8 June 2007. GPS IWV and HIRLAM IWV are observed at the GPS site in the center of the square in Fig. 1. The difference in temporal resolution is obvious. Figure 3 shows large deviations between GPS IWV and HIRLAM IWV that sometimes increase with forecast time; this has been noted before (see, e.g., Smith et al. 2007; de Haan and Barlag 2004, chapter 6.1). Furthermore, the GPS IWV and radiosonde observation are close except at 0000 UTC 9 June, for which time it deviates from both the HIRLAM analyses and the GPS value. In general, HIRLAM analyses are close to the observed GPS IWV (except the analysis at 0000 UTC 8 June). The forecasts show much larger discrepancies, especially the forecasts valid at 1200 UTC. At this time the GPS and radiosonde match perfectly. From 1500 to 1600 UTC, maximum radar reflectivity is observed up to nearly 63 dBZ (observed in a period of 5 min) in the area of 50 $\times$ 50 km^2. A reflectivity of 55 dBZ corresponds to a rain rate of approximately 100 mm h^{-1}. In the same period, a maximum of 500 discharges in 5 min is observed. These occurrences overlap a local increase of IWV from approximately 31 to 35 kg m^{-2}. This increase in IWV was present in the HIRLAM forecast started at 0600 and 1200 UTC. The first forecast started with a too-large amount of IWV, and the second overestimated the increase from 1500 to 1800 UTC.

Figure 3 shows an increase in IWV, but this happens after the time during which the thunderstorm appeared. The occurrence of the lightning around 1600 UTC seems to match with the increase in IWV. From the time series shown in Fig. 3 the thunderstorm event cannot be explained; two-dimensional representation may reveal the explanation for the occurrence of this thunderstorm when the observed two-dimensional water vapor field is

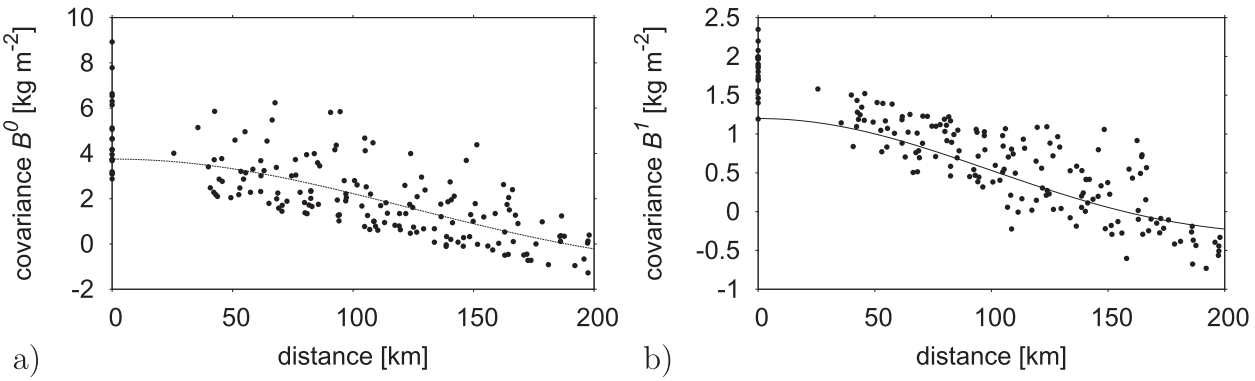

FIG. 2. Background error covariance with (a) a mean background and (b) a persistence background with respect to site separation.

of sufficient quality, as will be shown in section 4b; we will return to this case in section 5a.

b. *Quality of GPS integrated water vapor fields*

The accuracy of GPS IWV is typically around 5%–10% of the IWV value, when compared with radiosonde and NWP (Rocken et al. 1993, 1995, 1997; Emardson et al. 1998, 2000; Liou et al. 2001; Niell et al. 2001; Stoew et al. 2001; Guerova et al. 2003). Over the period 1 May–1 July 2007, the constructed IWV analyses are compared with estimates from GPS, radiosonde, and NWP. First, IWV estimates obtained from GOP are considered. Table 2 shows the statistics for the comparison of the two-dimensional analysis with the GPS solutions for three sites (see open squares in Fig. 1).

The IWV standard deviations were largest at sites with large distance to the closest GPS site used in the analysis (TERS). This is not surprising, because there is no IWV information available near this site. The bias and standard deviation at the two other sites are comparable. In comparison with GPS IWV from a different source, the standard deviation is around 2 kg m^{-2}.

The comparison with radiosonde observations from De Bilt shows very good correlation. A total of 96 comparisons at 0000 and 1200 UTC resulted in a negligible bias (0.01 kg m^{-2}) and a standard deviation of 1.94 kg m^{-2}.

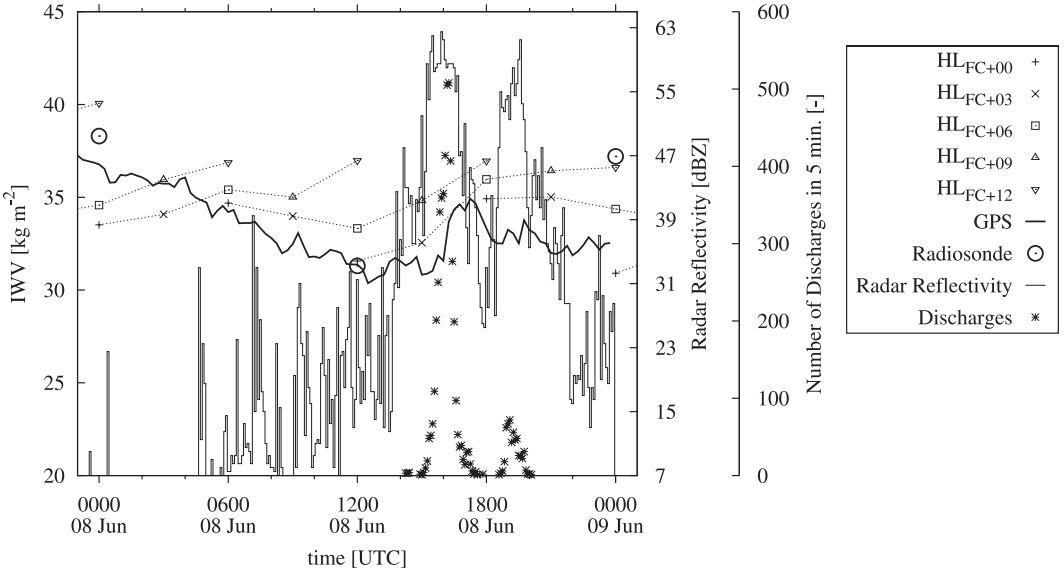

FIG. 3. Time series of IWV from GPS (thick line), radiosonde (circles), and HIRLAM IWV analysis and forecasts in De Bilt (dashed lines). Maximum radar reflectivity as observed by the radar in a 50 × 50 km^2 area is depicted by a thin solid line. The asterisks denote the number of discharges in the same area; the location of the area is shown in Fig. 1.

TABLE 2. Statistics of the difference between the analyzed IWV field (IWV_{an}) and GPS estimates from GOP over a period from May to June 2007.

Site	No.	$\overline{IWV_{an}}$ (kg m^{-2})	Bias (kg m^{-2})	σ (kg m^{-2})
DELF	1342	21.23	−0.25	2.08
EIJS	1344	22.32	−0.62	1.87
TERS	1343	19.85	−0.22	2.50

TABLE 3. Statistics of the difference between GPS and NWP IWV fields for different forecast lengths over a period from May to June 2007. The mean value of IWV_{an} is 21.77 kg m^{-2}.

Forecast length (h)	No.	Bias (kg m^{-2})	σ (kg m^{-2})
00	206	−0.44	2.01
03	206	−0.55	2.09
06	206	−0.43	2.20
09	206	−0.49	2.35
12	206	−0.38	2.46
24	206	−0.25	3.02
36	206	−0.01	3.61
48	206	0.19	4.00

When the analyzed IWV field is compared with the NWP field for the period from 1 May to 1 July for different forecast periods, the biases show no tendency and are around −0.5 kg m^{-2} (see Table 3) for the forecast lengths shorter than 12 h; for forecast lengths longer than 12 h, an increase in bias is observed. Note that the comparison is made on the validation region close to the sites (see Fig. 1). The IWV value for the analysis was determined by a weighted mean of four surrounding HIRLAM grid points. The statistics are determined using the HIRLAM grid points. The standard deviation shows an increase with forecast length of nearly 100% after 48 h. An increase in standard deviation is not surprising because an NWP forecast model always loses quality with increasing forecast length. Part of this increase in standard deviation is due to phase errors in the forecasts, resulting in a double penalty. Nevertheless, the sudden change in bias cannot be explained fully by the double-penalty argument.

We use a variational assimilation method instead of a simple bilinear interpolation scheme. The bias of a bilinear interpolation with NWP analysis was 5% more negative than the bias of the variational analysis. The standard deviation increased by 10% when a bilinear interpolation was used instead of a variational analysis. The advantage of bilinear interpolation is that it is fast, but the disadvantage is that when the GPS IWV at a certain site is not available (or is erroneous) the resulting IWV map could be unrealistic. Using a variational technique, which requires a background, this problem can be avoided.

In Fig. 4, the horizontal distribution of the mean IWV_{an} and the bias and standard deviation of the difference between IWV_{an} and HIRLAM analyses for June 2007 are shown. The signature of the bias between model and GPS analysis has a number of origins. The main cause of the difference is that the model orography and the GPS observation heights are different. The observations are taken as is, which implies that for a GPS receiver on a tall building the total amount of water vapor in the column will be lower than when the GPS receiver is installed at the surface. The horizontal representativeness of the GPS IWV value will also be smaller in areas of variable orography (see the increase in bias at the right-bottom corner in Fig. 4b). Systematic biases may be present in both model and GPS. Note that although there are no observations over the North Sea the bias against the model is small. Over land, the bias increases with distance to the coast, a result that could be related to an orographic signal. The standard deviation increases with increasing distance to the GPS network. This is clearly visible in the top-left and the bottom-right corners of Fig. 4. The overall bias ranges between 1.8 and 2.4 kg m^{-2}.

Figure 5 shows a time series of the mean IWV_{an}, the bias, and the standard deviation of the difference between the GPS IWV analysis and the NWP analysis and 6-h forecast (denoted as FC+00 and FC+06, respectively). Both the bias and standard deviation differ from time to time and even between the analysis and the forecast. In particular, during 7 and 8 June the biases of the analysis and forecast have opposite signs. On 20 and 21 June, the standard deviation of the 6-h forecast was significantly higher than the standard deviation of the NWP analysis and the biases were also of opposite sign. Note that because of problems in the GPS data exchange there are a few gaps in the time series.

The NWP analysis is created without GPS information: both fields can be regarded as being independent. It is apparent that the mean difference and standard deviation signal show that GPS IWV contains other information structures than does NWP and because GPS IWV observations are accurate the IWV_{an} is expected to have an additional value.

Figure 6 displays the frequency distribution of IWV in 4 kg m^{-2} bins for the period May–June of 2007. Figure 6a shows these distributions for radiosonde, NWP, and IWV_{an} at 0000 and 1200 UTC. Outside the range 16–24 kg m^{-2}, these distributions do not differ much. Both the NWP analysis and 6-h forecast show a different maximal distribution for values between 20 and 24 kg m^{-2}. The distribution of the NWP analysis differs less from the radiosonde distribution because the

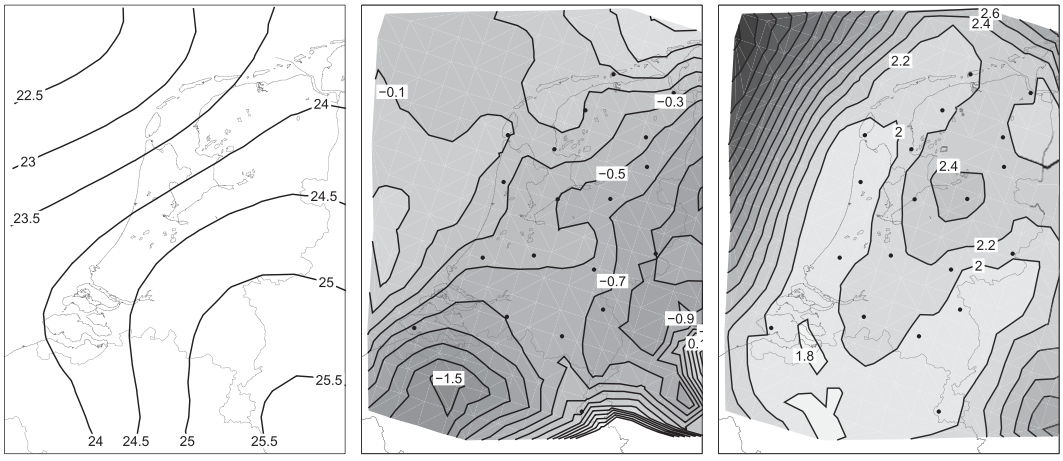

FIG. 4. (a) Mean of IWV_{an}, and (b) bias and (c) standard deviation of the difference between IWV_{an} and HIRLAM analysis for June 2007.

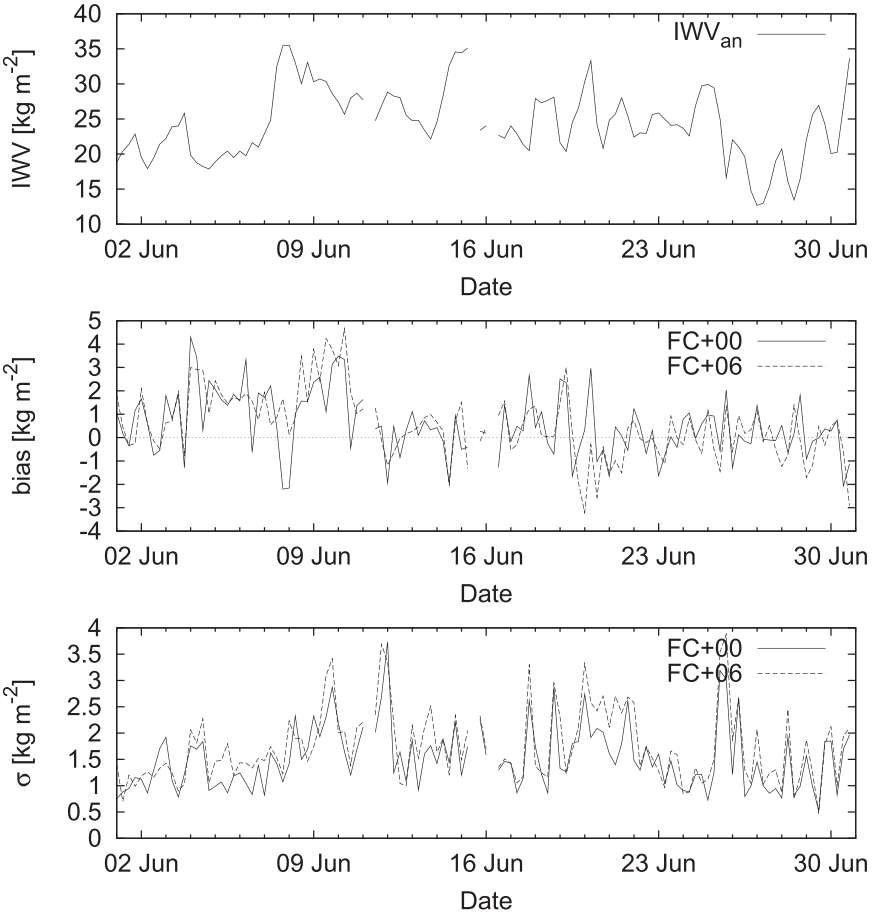

FIG. 5. Time series of the bias and standard deviation of the difference between GPS IWV analysis and NWP analysis (FC+00; solid line) and 6-h forecast (FC+06; dashed line), respectively.

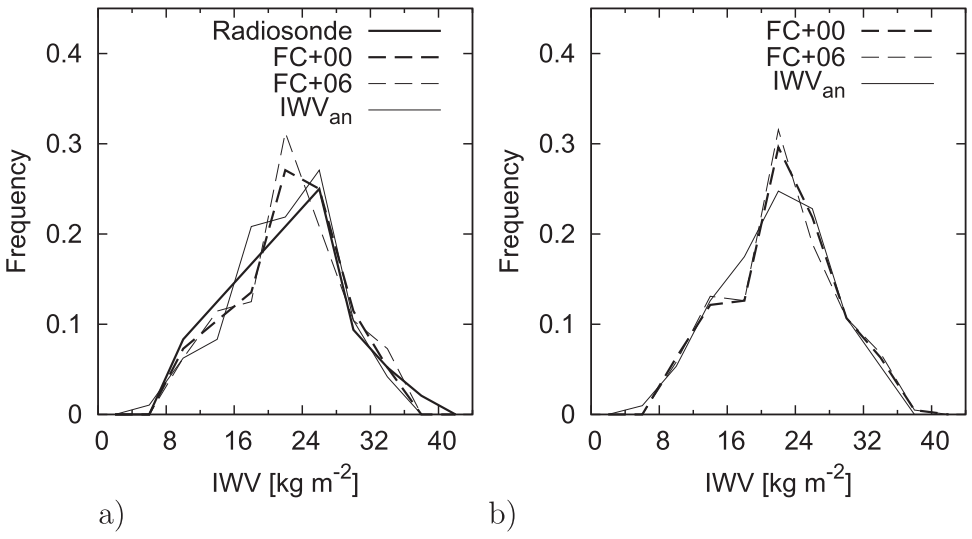

FIG. 6. Frequency distribution of IWV during May–June 2007 from radiosonde (thick solid line), NWP analysis and 6-h forecast (thick and thin dashed lines, respectively), and GPS-IWV analysis (thin solid line). Shown are the distributions for (a) 0000 and 1200 UTC and (b) 0000, 0600, 1200, and 1800 UTC. Note that no radiosondes are launched at 0600 and 1800 UTC at De Bilt.

information of these observations is assimilated in the NWP analysis; however, the difference is remarkable. The distributions of the radiosonde and IWV_{an} are very close. Figure 6b shows the distributions for all available times (0000, 0600, 1200, and 1800 UTC). Outside 16–24 kg m^{-2}, the distributions are almost identical. For values between 16 and 24 kg m^{-2} there is a shift in distribution: the NWP dataset contains fewer observations between 16 and 20 kg m^{-2} than does GPS. This difference in water vapor distributions from NWP can also be observed in Fig. 6a, although it is less apparent. The reason for this shift in IWV values needs further investigation.

5. Application to nowcasting cases

a. A severe thunderstorm on 8 June 2007

On 8 June 2007 a low pressure system moved toward the Netherlands from the southeast. Pressure values of 1012 hPa were observed in the center of this system: the low pressure system was not well developed. Nevertheless, a local severe-weather event occurred around 1400 UTC on the eastern part of the border between the Netherlands and Belgium, causing flooding in Maastricht. The thunderstorm produced rain rates that were between 10 and 30 mm h^{-1} and over 200 lightning discharges in a 10×10 km^2 area. A very unstable profile was observed by the radiosonde observation from De Bilt at 1200 UTC. The lifting condensation level (LCL) was around 900 hPa, and the level of neutral buoyancy (LNB) was around 200 hPa. The Boyden index, defined as $BI = 0.1(z_{700} - z_{1000}) - T_{700} - 200$ (Boyden 1963), was around 98. The Boyden index appears to be a good indicator for thunderstorm intensity: values exceeding 96 are an indicator for severe thunderstorm activity (Schmeits et al. 2005). Haklander and van Delden (2003) showed also that the Boyden index, even though it does not account for any moisture, serves surprisingly well as a dichotomous thunderstorm predictor.

There was very little wind shear at 850 hPa where the wind direction turned from southwest to more southerly. The surface winds at 1400 UTC show that there is a convergence zone right at the location of the thunderstorm. To the west of the convergence zone, surface winds are from the west to northwest; east of the convergence zone winds blow from the east. A dry tongue of IWV lies over the Netherlands at 1400 UTC with low values (23 kg m^{-2}) in the mideast of the Netherlands and strong gradients toward the south and west. Figure 7 shows the observed surface winds (wind barbs), GPS IWV (contours), radar rain rates (grayscale), and lightning events (symbols) for four times starting at 1400 UTC, with a time step of 1 h.

Surface relative humidity observations had no added value in this case. These observations are representative of the lowest part of the boundary layer only.

The heavy rainfall and intense lightning activity occur right at the convergence zone of the surface wind. Air with a large amount of IWV is advected from the west to this region; air from the east contains less moisture. Note that surface winds are not representative of winds

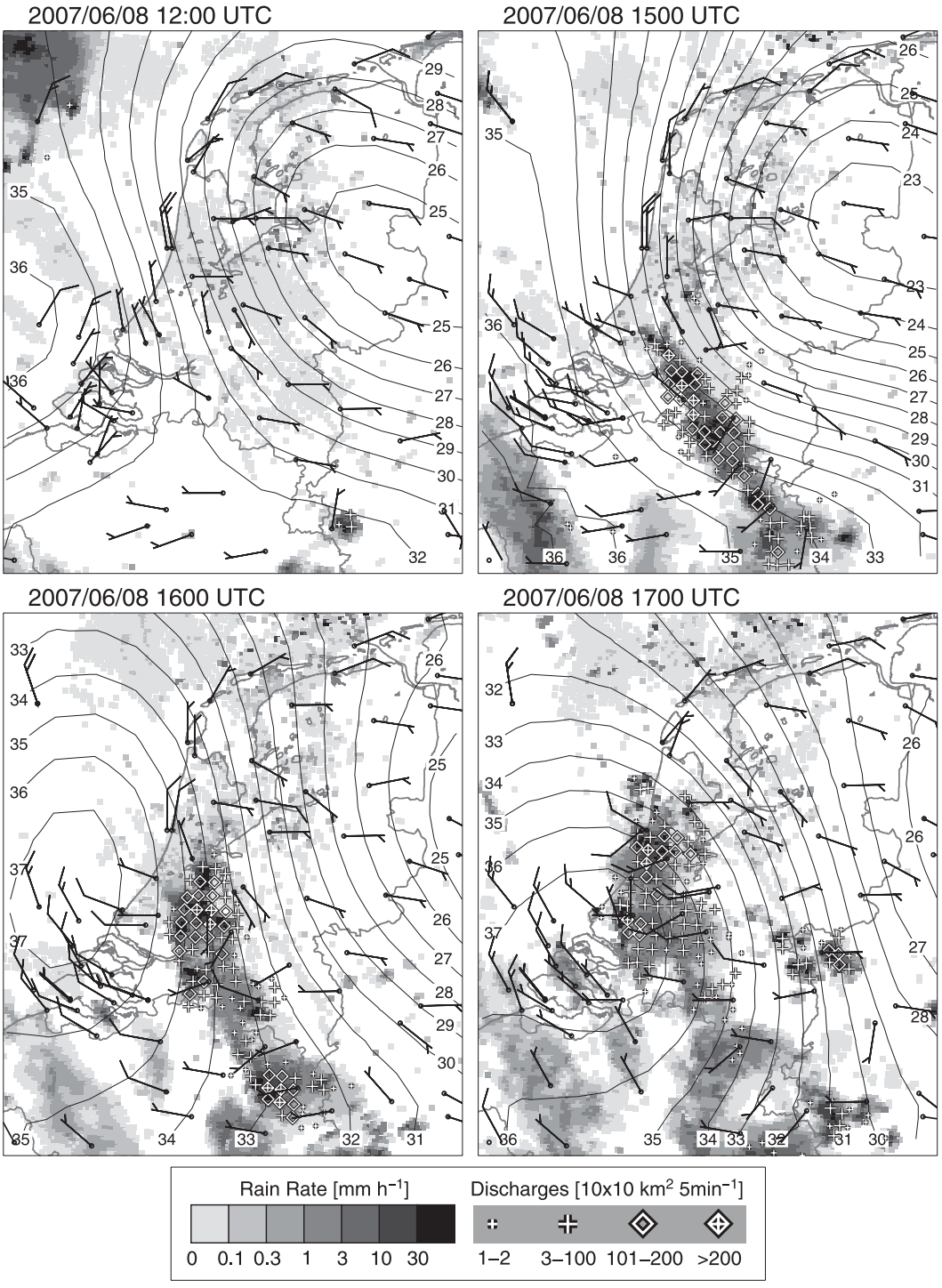

FIG. 7. Radar rain-rate observations (grayscale), lightning discharges (crosses and diamonds), GPS IWV (contours), and surface wind observations (wind barbs) at 1200 and 1500–1700 UTC 8 Jun 2007.

at higher altitudes. However, most moisture resides in the lower part of the atmosphere. The convergence of the moisture increased the activity of the thunderstorm, which is clearly visible from the GPS IWV maps.

b. Two thunderstorm events on 20 July 2007

The second case describes the occurrence of two thunderstorms. A low pressure system moved northeastward

through the English Channel toward the Netherlands on 20 July 2007. A warm front, on the east side of the system with an east–west direction, preceded the low pressure system. On the west side of the low pressure center an occulted front moved to the west. At 1800 UTC this system was situated over the mideast of the Netherlands. The radiosonde profile from De Bilt at 1200 UTC showed an almost completely saturated profile with an LCL at 950 hPa and an LNB around 290 hPa. The Boyden index was 96, which implies a moderate chance of severe thunderstorms. Surface winds ahead of the low pressure system were from the northeast; behind this system southwest winds were observed. A water vapor maximum traveled from south to north over the Netherlands, entering the south at 1000 UTC and leaving the region at 1900 UTC. The maximum value was over 40 kg m^{-2}. A large thunderstorm moved in the same direction, although with a higher group velocity; the maximum activity occurred east of the water vapor maximum. The thunderstorm entered the Netherlands at 1100 UTC and had exited the country by 1700 UTC. At that time a second line of thunderstorms developed over the middle of the Netherlands; the position of this thunderstorm coincides locally with water vapor contours at the location where the water vapor gradients are large. In Fig. 8, the observed surface winds (wind barbs), GPS IWV (contours), radar rain rates (grayscale), and lightning events (symbols) for four times, with a time step of 2 h, are shown. Also, in this case the surface relative humidity observations showed no signal for the occurrence of the thunderstorms.

It appears that the intense lightning of the first thunderstorm occurred to the east of the water vapor maximum. The thunderstorm overtook the water vapor maximum and then weakened. The second thunderstorm developed in a zone of surface wind convergence that was present more than 2 h prior. Moist air was advected from the maximum (which lies north of the convergence zone) to this region, resulting in an increase in the intensity of the thunderstorm (Banacos and Schultz 2005). Thus again, the IWV fields provide useful information.

c. Intense line of lightning on 31 May 2008

The last case presented here describes the occurrence of an intense line of thunderstorms that were aligned with (or through) the general atmospheric flow. On 31 May 2008 a moderate high pressure system was present over western Europe, extending from England to Germany. Radiosonde observations at 1200 UTC 31 May show a surface wind from the northwest while above 800 hPa the wind veered toward the east. This profile had a Boyden index of 94 and was unsaturated. At 0000 UTC 1 June 2008 the radiosonde launch showed that the winds at high altitude where still from the east while in the boundary layer the winds were from the southeast. The profile was almost completely saturated from 900 up to 400 hPa. The Boyden index was again around 94.

The water vapor distribution at 1800 UTC showed a wet tongue that lay over the central east of the Netherlands (see Fig. 9). This wet tongue sharpened a little within the next few hours but was stationary until 2100 UTC. A strong water vapor gradient ran from the central east with a curve toward the north. The overall surface wind direction was from the north, except for the central area around the strong gradient; there, the winds were turning anticlockwise around the water vapor maximum. The line of thunderstorms started to appear around 2000 UTC 31 May and was present to around 0000 UTC 1 June.

Although the BI did not give an indication of the occurrence of a thunderstorm, a line formation of thunderstorms appeared right at the southern water vapor gradient. From 2100 UTC onward, the water vapor tongue was advected over the Netherlands, decreasing its gradient, and eventually the thunderstorm activity decreased as well. The surface winds around this gradient created a convergence zone of moisture, increasing the instability of the atmosphere. Again, the integrated water vapor maps gave an indication of areas of local instability a few hours prior to the occurrence.

6. Conclusions

In this paper a method is presented for constructing real-time two-dimensional water vapor maps from integrated water vapor observations obtained from a surface network of GPS receivers. The analysis method is based on a two-dimensional variational technique with a persistence background. Every variational analysis system requires knowledge about the observation and background error covariances. The observation error covariances are assumed to be uncorrelated between different locations. Background error covariances are determined based on the Hollingsworth–Lonnberg method (Hollingsworth and Lonnberg 1986). The method described in this paper uses a two-step technique to avoid the use of a forward model. In the first step the background map is retrieved from an independent GPS data source valid at the same time of observation over a period from January to July of 2007. The difference between the mean value of the region under consideration and the observed real-time GPS IWV observations determines the first set of background

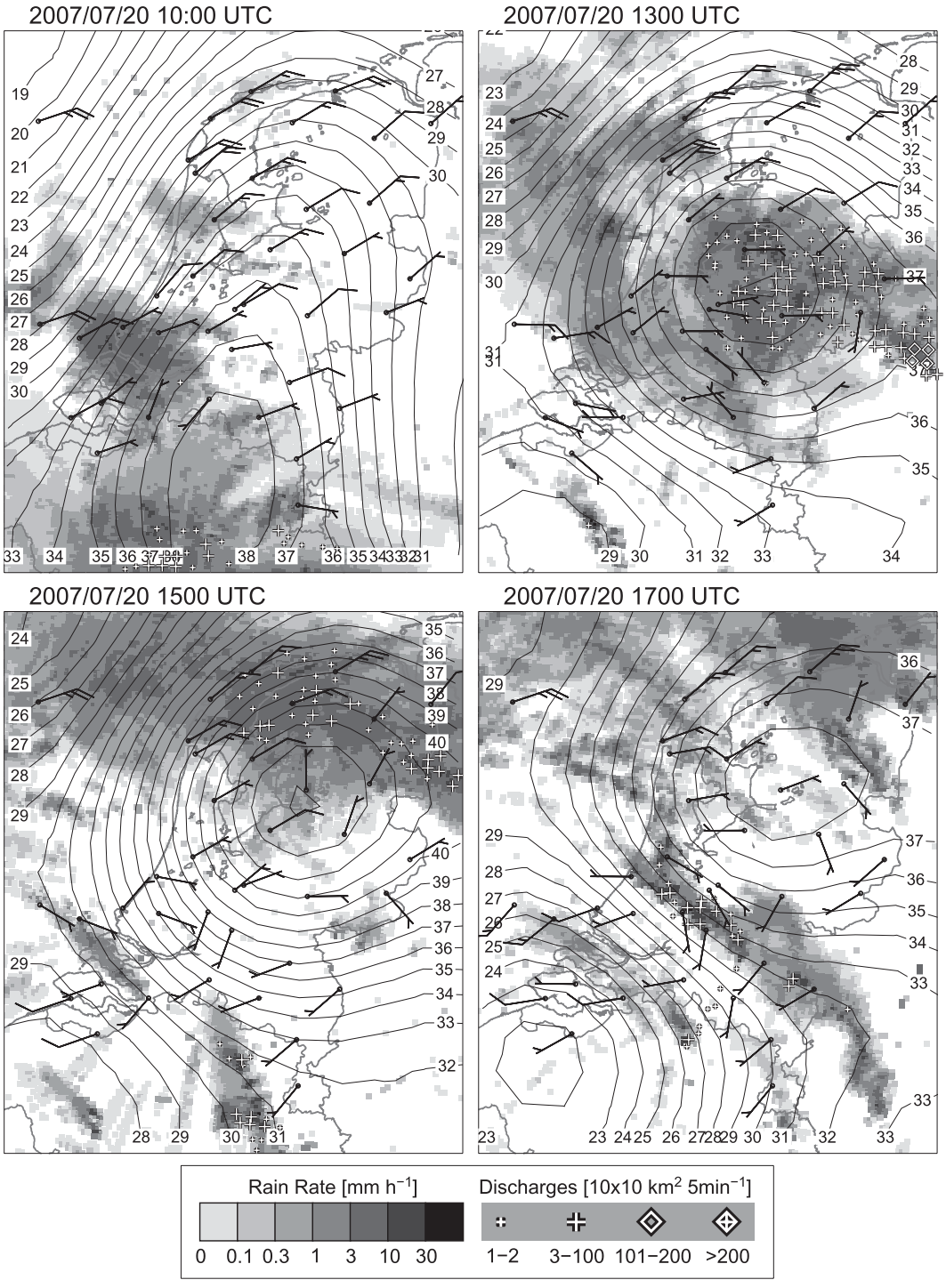

FIG. 8. As in Fig. 7, but at 1000, 1300, 1500, and 1700 UTC 20 Jul 2007.

error covariances. Next, these background error covariances are used together with real-time observations to obtain an analysis map. This map is then used to determine the background error covariances with real-time observation 15 min later.

The maps are validated with HIRLAM IWV analysis and forecast maps and with radiosonde observations. The mean difference between radiosonde and GPS IWV maps is negligible, and the standard deviation is less than 2 kg m^{-2}. The bias between HIRLAM and

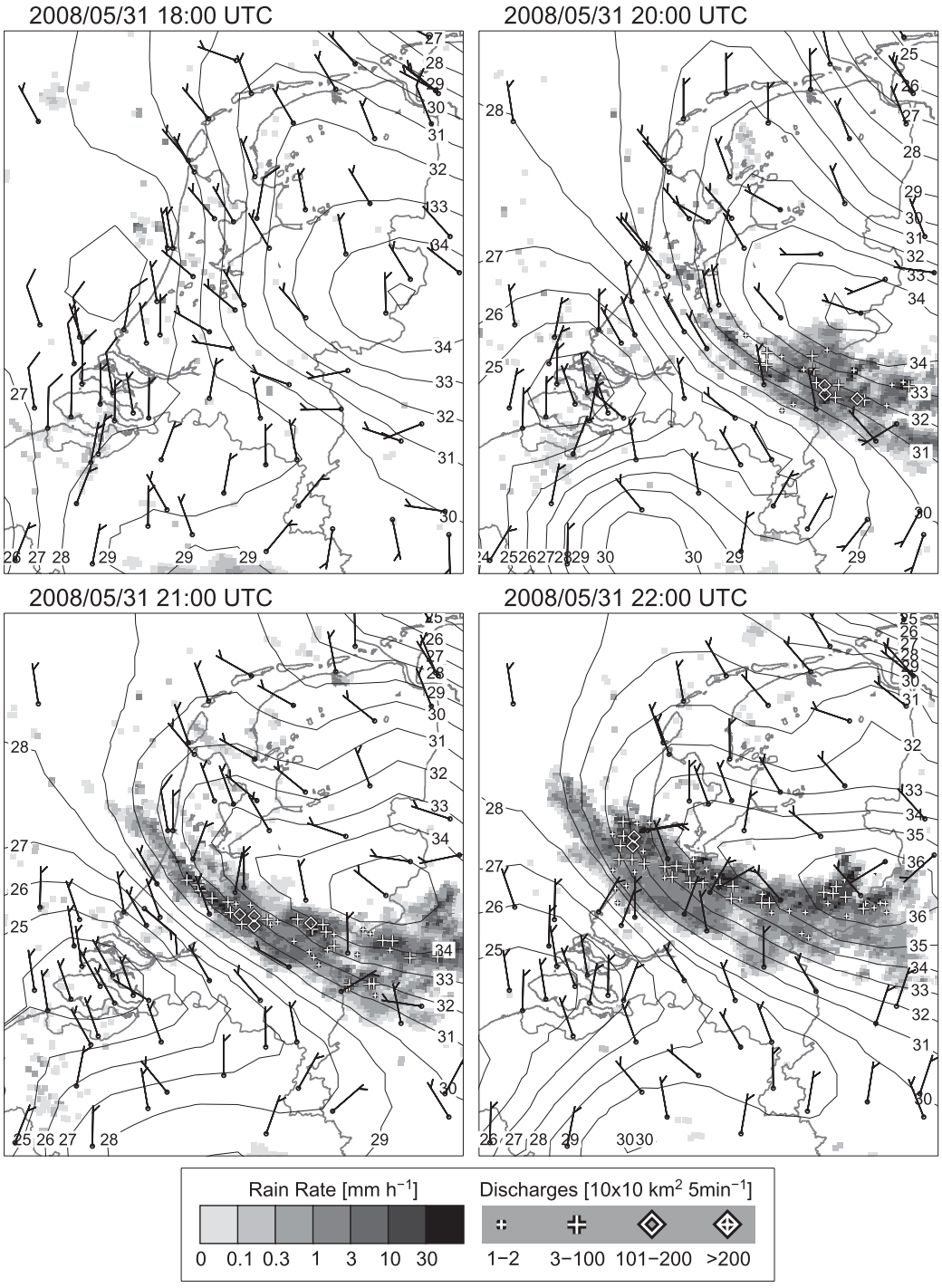

FIG. 9. As in Fig. 7, but at 1800 and 2000–2200 UTC 31 May 2008.

GPS IWV is between 0.4 and 0.6 kg m^{-2}, and the standard deviation increases from 2 to 4 kg m^{-2} with increasing forecast length to 48 h. This is due to the fact that the forecast skill decreases with increasing forecast length. The horizontal distribution of the difference between 1 month of HIRLAM IWV and GPS IWV shows a small signal of increasing bias with increasing distance to the coast. The standard deviation increases dramatically with increasing distance from the observation network. Histograms of the IWV values of HIRLAM are different from those observed with radiosonde and GPS. The occurrence of IWV values

around 16 kg m^{-2} and around 20 kg m^{-2} for HIRLAM seems to be shifted toward the higher values relative to both radiosonde and GPS. The statistics are representative for a larger period, because GPS IWV observations have a standard deviation of 5%–10% over all seasons when compared with radiosondes, water vapor radiometer observations, and NWP.

By examining three cases, the additional value of the real-time GPS IWV maps for nowcasting is illustrated. All cases show that the convergence of moist air contains information about the location of developing thunderstorms. In the future we plan to perform an evaluation of real-time GPS IWV maps over a whole season.

Altogether it is concluded that the real-time GPS IWV maps constructed using a two-dimensional variational method are of good quality and can be helpful for nowcasting of severe thunderstorms.

Acknowledgments. The authors thank the GPS data providers within the EUREF Permanent Network (EPN) and the International GNSS Service (IGS) for giving access to their data and products. Special thanks are given to the Bundesamt für Kartographie und Geodäsie (BKG), Frankfurt am Main, Germany, for access to the real-time GPS data (NTRIP). The development of the real-time processing scheme of GPS data was sponsored by The Netherlands Agency for Aerospace Programmes (NIVR).

REFERENCES

Baltink, H. K., H. van der Marel, and A. G. A. van der Hoeven, 2002: Integrated atmospheric water vapor estimates from a regional GPS network. *J. Geophys. Res.,* **107,** 4025, doi:10.1029/2000JD000094.

Banacos, P., and D. Schultz, 2005: The use of moisture flux convergence in forecasting convective initiation: Historical and operational perspectives. *Wea. Forecasting,* **20,** 351–366.

Beekhuis, H., and I. Holleman, 2004: Upgrade and evaluation of a lightning detection system. *Proc. Int. Lightning Detection Conf. 2004,* Helsinki, Finland, Vaisala, 17 pp.

Bevis, M., S. Businger, S. Chiswell, T. A. Herring, R. A. Anthes, C. Rocken, and R. H. Ware, 1994: GPS meteorology: Mapping zenith wet delays onto precipitable water. *J. Appl. Meteor.,* **33,** 379–386.

Boyden, C. J., 1963: A simple instability index for use as a synoptic parameter. *Meteor. Mag.,* **92,** 198–210.

Daley, R., 1991: *Atmospheric Data Analysis*. 2nd ed. Cambridge University Press, 457 pp.

Davis, J., T. Herring, I. Shapiro, A. Rogers, and G. Elgered, 1985: Geodesy by radio interferometry: Effects of atmospheric modeling errors on estimates of baseline length. *Radio Sci.,* **20,** 1593–1607.

de Haan, S., 2006: Measuring atmospheric stability with GPS. *J. Appl. Meteor. Climatol.,* **45,** 467–475.

——, and S. J. M. Barlag, 2004: Time series. *Final Report of COST716 Working Group 1,* G. Elgered et al., Eds., European Union, 98–103.

——, H. van der Marel, and S. J. M. Barlag, 2002: Comparison of GPS slant delay measurements to a numerical model: Case study of a cold front passage. *Phys. Chem. Earth,* **27,** 317–322.

——, S. J. M. Barlag, H. K. Baltink, and F. Debie, 2004: Synergetic use of GPS water vapor and Meteosat images for synoptic weather forecasting. *J. Appl. Meteor.,* **43,** 514–518.

Doviak, R. J., and D. S. Zrnić, 1993: *Doppler Radar and Weather Observations*. 2nd ed. Academic Press, 562 pp.

Emardson, T. R., G. Elgered, and J. M. Johanson, 1998: Three months of continuous monitoring of atmospheric water vapor with a network of global positioning system receivers. *J. Geophys. Res.,* **103,** 1807–1820.

——, J. M. Johanson, and G. Elgered, 2000: The systematic behaviour of water vapor estimates using four years of GPS observations. *Trans. IEEE Geosci. Remote Sens.,* **GE-3,** 324–329.

Guerova, G., E. Brockmann, J. Quiby, F. Schubiger, and C. Mätzler, 2003: Validation of NWP mesoscale models with Swiss GPS network AGNES. *J. Appl. Meteor.,* **42,** 141–150.

Haklander, A. J., and A. van Delden, 2003: Thunderstorm predictors and their forecast skill for the Netherlands. *Atmos. Res.,* **67–68,** 273–299.

Holleman, I., 2005: Quality control and verification of weather radar wind profiles. *J. Atmos. Oceanic Technol.,* **22,** 1541–1550.

——, 2007: Bias adjustment and long-term verification of radar-based precipitation estimates. *Meteor. Appl.,* **14,** 195–203.

——, H. Beekhuis, S. Noteboom, L. Evers, H. W. Haak, H. Falcke, and L. Bähren, 2006: Validation of an operational lightning detection system. *Proc. Int. Lightning Detection Conf. 2006,* Tucson, AZ, Vaisala, 16 pp. [Available online at http://www.vaisala.com/files/Validation_of_an_operational_lightning_detection_system.pdf.]

Hollingsworth, A., and P. Lonnberg, 1986: The statistical structure of short-range forecast errors as determined from radiosonde data. Part I: The wind field. *Tellus,* **38A,** 111–136.

Liou, Y. A., Y. T. Teng, T. van Hove, and J. C. Liljegren, 2001: Comparison of precipitable water observations in the near tropics by GPS, microwave radiometer, and radiosondes. *J. Appl. Meteor.,* **40,** 5–15.

Macpherson, S. R., G. Deblonde, J. M. Aparicio, and B. Casati, 2007: Impact of ground-based GPS observations on the Canadian Regional Analysis and Forecast System. Preprints, *11th Symp. on Integrated Observing and Assimilation Systems for the Atmosphere, Oceans, and Land Surface (IOAS-AOLS),* San Antonio, TX, Amer. Meteor. Soc., 5.5. [Available online at http://ams.confex.com/ams/pdfpapers/117995.pdf.]

Marshall, J. S., and W. M. Palmer, 1948: The distribution of raindrops with size. *J. Meteor.,* **5,** 165–166.

Mazany, R. A., S. Businger, S. I. Gutman, and W. Roeder, 2002: A lightning prediction index that utilizes GPS-integrated precipitable water vapor. *Wea. Forecasting,* **17,** 1034–1047.

Niell, A. E., A. J. Coster, F. S. Solheim, and V. B. Mendes, 2001: Comparison of measurements of atmospheric wet delay by radiosonde, water vapor radiometer, GPS, and VLBI. *J. Atmos. Oceanic Technol.,* **18,** 830–850.

Poli, P., and Coauthors, 2007: Forecast impact studies of zenith total delay data from European near real-time GPS stations in Météo France 4DVAR. *J. Geophys. Res.,* **112,** D06114, doi:10.1029/2006JD007430.

Ray, R. D., 1999: A global ocean tide model from TOPEX/Poseidon altimetry: GOT99.2. NASA Tech. Memo. 209478, Goddard Space Flight Center, 58 pp.

Rocken, C., R. Ware, T. van Hove, F. Solheim, C. Alber, J. Johnson, M. Bevis, and S. Businger, 1993: Sensing atmospheric water

vapor with the global positioning system. *Geophys. Res. Lett.,* **20,** 2631–2634.

——, T. van Hove, J. Johnson, F. Solheim, R. Ware, M. Bevis, S. Chiswell, and S. Businger b, 1995: GPS/STORM—GPS sensing of atmospheric water vapor for meteorology. *J. Atmos. Oceanic Technol.,* **12,** 468–478.

Rocken, C. R., T. van Hove, and R. H. Ware, 1997: Near real-time GPS sensing of atmospheric water vapor. *Geophys. Res. Lett.,* **24,** 3221–3224.

Saastamoinen, J., 1972: Atmospheric correction for the troposphere and stratosphere in radio ranging of satellites. *The Use of Artificial Satellites for Geodesy, Geophys. Monogr.,* Vol. 15, Amer. Geophys. Union, 247–251.

Scherneck, H.-G., 1991: A parametrized solid earth tide mode and ocean loading effects for global geodetic base-line measurements. *Geophys. J. Int.,* **106,** 677–694.

Schmeits, M. J., K. J. Kok, and D. H. P. Vogelezang, 2005: Probabilistic forecasting of (severe) thunderstorms in the Netherlands using model output statistics. *Wea. Forecasting,* **20,** 134–148.

Smith, T. L., S. I. Gutman, and S. R. Sahm, 2007: Forecast impact from assimilation of GPS IPW observations into the Rapid Update Cycle. *Mon. Wea. Rev.,* **135,** 2914–2930.

Stoew, B., G. Elgered, and J. M. Johansson, 2001: An assessment of estimates of integrated water vapour from ground based GPS data. *Meteor. Atmos. Phys.,* **77,** 99–107.

Undén, P., and Coauthors, 2002: HIRLAM-5 scientific documentation. IRLAM Project Tech. Rep., Norrköping, Sweden, 144 pp. [Available online at http://hirlam.org.]

Vaisala, 2006: Vaisala radiosonde RS92-SGP brochure. Vaisala Oyj Tech. Rep. Ref. B210358EN-C, Helsinki, Finland, 2 pp. [Available online at http://www.vaisala.com/.]